

Use of Particle-Tracking Velocimetry and Flow Birefringence To Study Nonlinear Flow Behavior of Entangled Wormlike Micellar Solution: From Wall Slip, Bulk Disentanglement to Chain Scission

Pouyan E. Boukany and Shi-Qing Wang*

Department of Polymer Science, University of Akron, Akron, Ohio 44325

Received November 13, 2007; Revised Manuscript Received December 2, 2007

ABSTRACT: In this work, we have investigated nonlinear flow behavior of an entangled living polymer solution made of wormlike micelles of cetyltrimethylammonium bromide (CTAB) and sodium salicylate (NaSal), using a combination of rheometric, particle tracking velocimetric (PTV), and flow birefringence (FB) techniques. The responses of the entangled micellar solution to various modes of shear including startup, creep, large-amplitude oscillatory shear (LAOS), and step shear are analyzed with PTV and FB. Apart from the usual nonlinear behavior analogous to that observed in entangled polymer solutions, i.e., shear inhomogeneity in the form of either interfacial slip or nonlinear velocity profile in the bulk that is plausibly due to deformation-induced chain disentanglement, the entangled micellar solution shows a sign of molecular rupture (i.e., chain scission) when it is subjected to a high rate of shear beyond a critical strain level of 4.0. LAOS at amplitude of 6.0 produces a similar rupture in the sample interior. On the other hand, creep flow can avoid such rupture, allow development of less sharp boundaries among the different layers of varying local shear rates, and still reach high apparent rates. Finally, application of FB observations not only confirms the PTV measurements of shear inhomogeneity but also reveals structural nonuniformity in the flow–vorticity plane both during a startup shear and in relaxation after a large step shear.

I. Introduction

Self-assembly of surfactants into chainlike micelles¹ presents an interesting case where the “polymerization” is reversible in aqueous solutions. At appropriate concentrations in the presence of salt, wormlike micelles can grow into such long linear chains that they can be imaged with fluorescence microscopy.² At sufficiently high concentrations, wormlike micelles form an entanglement network and show viscoelastic behavior resembling that of entangled polymer solutions.³ Such wormlike micellar solutions have stimulated considerable experimental and theoretical interests as they are known to be almost Maxwell-like with a single relaxation time,^{4,5} display a stress plateau regime, and show nonlinear responses^{6–18} just beyond the terminal flow regime. Their low elastic modulus made it experimentally straightforward to explore nonlinear flow behavior without ambiguity.

Assuming that entangled wormlike micelles would behave like entangled polymer chains, Cates and co-workers extended¹⁹ an earlier theoretical analysis^{20,21} to conclude that the stress plateau character and shear banding are synonymous. For a long time, micellar solutions had been regarded as the only polymer-like system to possess convincing stress plateau.^{6,7} These earlier experimental and theoretical works evidently encouraged efforts to look for shear banding in such wormlike entangled micellar solutions. After initial flow birefringence and small-angle scattering measurements,^{22–31} velocity profiles were reported on the basis of NMR imaging to reveal inhomogeneous shear in these self-assembled fluids.^{32–42} These successes are remarkable, in contrast to the more difficult attempt to search for stress plateau like behavior in entangled polymer solutions. Although beyond the terminal regime there is a region where the slope

of shear stress vs imposed average rate is very small and thus could be taken as stress plateau like, previous experimental studies typically found the flow curve to be monotonic for entangled polymer solutions.^{43,44} This experimental situation generated an impression⁴⁵ that shear banding would not exist in entangled polymer solutions and deterred people for at least a decade from probing velocity profiles in the shear-thinning regime of entangled polymer solutions. It is against this background that recently revealed inhomogeneous shear under such commonly encountered conditions such startup shear and^{46,47} large-amplitude oscillatory shear (LAOS)^{48,49} came as a surprise. Particle-tracking velocimetric (PTV) observations^{50,51} of macroscopic recoil-like motions after a step strain were even more startling and have led to a new set of theoretical considerations.⁵²

Are entangled solutions made of wormlike micelles really the same as polymer solutions as far as their responses to various shearing conditions are concerned? In our view, an alternative microscopic mechanism for shear banding in micellar solutions may be plausible due to the character that the “polymer chains” are living, i.e., the wormlike micelles break and re-form constantly in solution. Because of this possibility, we did not previously think that shear banding in wormlike micellar solutions necessarily implies occurrence of inhomogeneous shear in entangled polymer solutions. This partially explains the 10-year gap between the first report of shear banding in entangled micellar solutions³² and that in entangled polymer solutions.⁴⁶

In the present study, we employ both particle tracking velocimetry (PTV) and flow birefringence (FB) visualization along with conventional rheometric measurements to explore nonlinear responses of an entangled wormlike micellar solution based on cetyltrimethylammonium bromide (CTAB) and sodium salicylate (NaSal) under various flow conditions ranging from startup shear, creep, LAOS to step strain. Several findings are

* Corresponding author. E-mail: swang@uakron.edu.

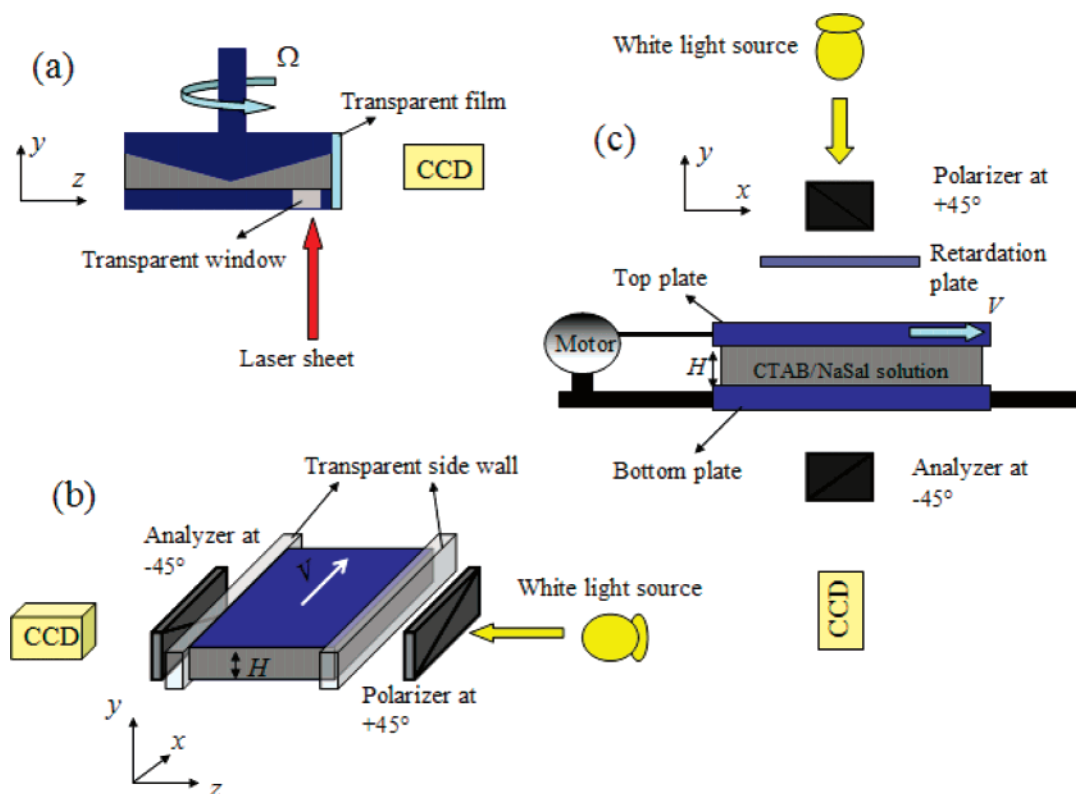


Figure 1. Depiction of the particle tracking velocimetric (PTV) and flow birefringence (FB) setups in cone-plate and parallel plate geometries (X , Y , Z axis is along flow, velocity gradient, and vorticity direction, respectively). (a) PTV setup in cone-plate geometry (25 mm, 4°) where a laser sheet illuminates the sample thickness and velocity profile is captured by a CCD camera. (b) FB setup along the velocity gradient Y direction. The incident white light passed through the crossed polarizer $+45^\circ$ and analyzer -45° to flow direction. (c) FB setup along the vorticity Z direction, where a retardation plate is placed between polarizer at $+45^\circ$ and analyzer -45° to flow direction.

new. (i) PTV observations reveal massive wall slip just beyond the terminal regime. (ii) Creep flow is seen to also produce shear banding. (iii) Although the same average rheological states can be produced by startup shear and creep, the actual inhomogeneous states are different. (iv) Startup shear at high rates appears to produce inhomogeneous states by causing micellar breakup instead of disentanglement. (v) The solution also undergoes inhomogeneous deformation during LAOS. (vi) A large step strain produces nonquiescent relaxation. (vii) The failure of the entanglement network during startup shear and after step shear is inhomogeneous not only along the velocity gradient direction but also in the flow-vorticity plane.

II. Experimental Section

Materials. This study is based on cetyltrimethylammonium bromide (CTAB) and sodium salicylate (NaSal) purchased from Sigma-Aldrich. The quality and degree of purity of chemicals were good enough without any further purification. We study a solution at a CTAB solution at a concentration of 0.1 M ($\phi_{\text{CTAB}} \sim 0.036$) and NaSal concentration of 0.07 M dissolved in distilled water. The prepared sample was kept for several days (at least 72 h) at room temperature to achieve equilibrium state, prior to experiments. Silver-coated particles (Dantec Dynamics HGS-10) were uniformly dispersed in the micellar solution at a low concentration (300–400 ppm) for the purpose of particle tracking velocimetric observations. To the best of our knowledge, these microparticles are uncharged.

Measurements. Rheological and PTV measurements were carried using a Physica MCR-301 rotational rheometer (Anton Paar) in a cone-plate setup. For conventional rheometric measurements, a cone of angle 2° and diameter 25 mm (CP-25 mm- 2°) is placed on top of a circular base of much larger diameter so that the meniscus can be surrounded by a low-molecular-weight poly(dimethylsiloxane) to prevent water evaporation. Each measurement

involved discrete fresh sample loading. All measurements took place at room temperature around 23°C .

Particle Tracking Velocimetric (PTV) Setup. In our PTV device, a sheet of laser passes across the sample thickness, and a charge-coupled device (CCD) camera captures movements of the illuminated particles, allowing a time-dependent velocity profile to be determined, as shown in Figure 1a. To observe the flow field inside the sample, a flexible transparent film is wrapped around the meniscus. Our observation plane is 3–4 mm from the meniscus. The setup involves a cone of angle 4° and diameter 25 mm placed above a 25 mm diameter disk (CP-25 mm- 4°), as depicted in Figure 1a. All measurements took place at room temperature around 23°C .

Flow Birefringence (FB) Setup. For flow birefringence observations, a sliding plate shear cell was built with two glass plates, and transparent side walls were used to contain the sample during shear so that FB observations can be conducted in either flow-vorticity or flow-gradient plane, as shown in parts b and c of Figure 1, respectively. In the first setup, a fiber-optic illuminator is used as the white light source. The incident white light travels horizontally from one side through the sample width between two crossed polarizers (at a 45° angle to the shear direction, X), and a color CCD camera (mounted with a variable magnification lens, Edmund VZM model 1000, No. 54396) captures the transmitted light from the other side. In the second FB setup shown in Figure 1c, the white light source is sent on the top transparent plate, and a color CCD camera is placed to receive the transmitted light from the bottom glass plate, where a full-wave retardation plate is placed (perpendicular to the shear direction) between two crossed polarizers that are at a 45° angle to flow direction (X). All measurements were carried out at room temperature around 23°C .

III. Results and Discussion

A. Linear Rheology. Figure 2 shows the magnitude of the complex viscosity, storage, and loss moduli from an oscillatory

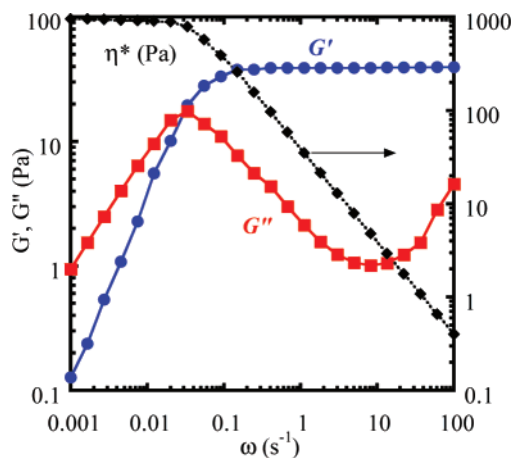


Figure 2. Complex viscosity η^* and storage and loss moduli G' and G'' vs frequency ω .

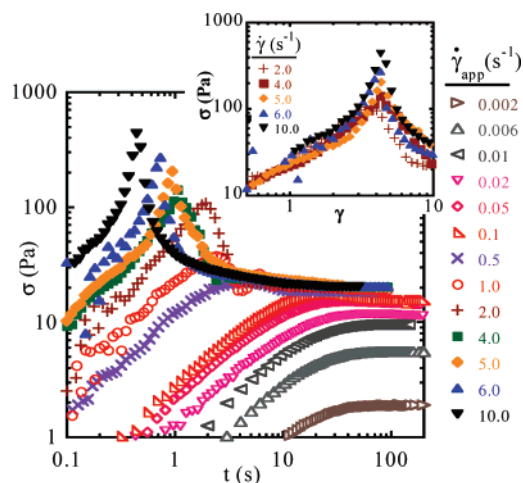


Figure 3. Growth of shear stress σ (Pa) as a function of time in startup shear at different imposed shear rates. The inset presented the growth of σ vs the elapsed strain γ for $\dot{\gamma}_{app}$ between 2 and 10 s^{-1} , where a cusp is clearly seen to occur at $\gamma = 4.0$ independent of the applied rate.

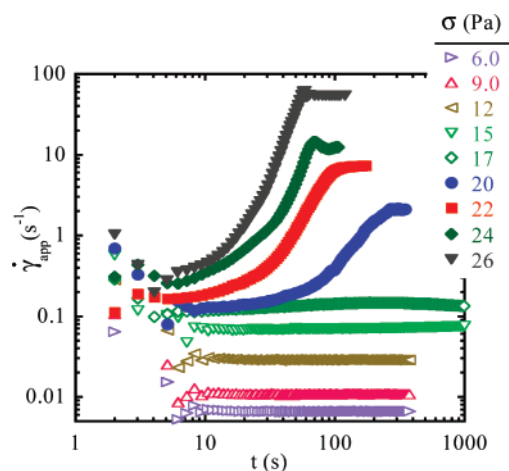


Figure 4. Changes of $\dot{\gamma}_{app}$ as a function of time in discrete creep experiments at various applied constant σ (Pa).

shear frequency sweep test at a low strain ($\sim 5\%$) at room temperature. The plateau modulus G_p of this sample is around 39 Pa and indeed very low relative to (by a factor of at least 10) the typical G_p of entangled polymer solutions,^{51,53} and the terminal relaxation time τ is around 31 s.

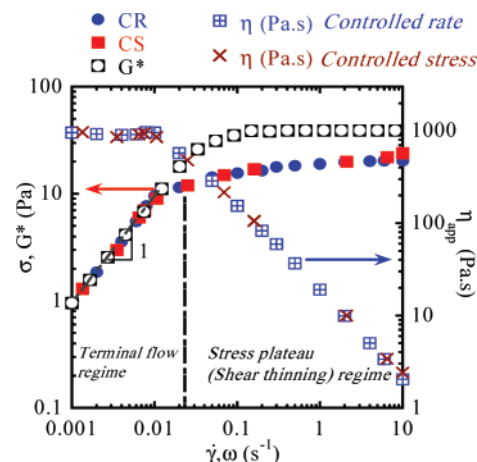


Figure 5. Flow curves of the CTAB/NaSal (0.1:0.07 mol/L) aqueous solution determined by small-amplitude oscillatory shear (SAOS), startup shear, and creep measurements with CP-25 mm-2°. The filled squares and circles represent the steady-state values of shear σ and $\dot{\gamma}_{app}$ from creep and startup shear, and open squares represent the complex modulus G^* from SAOS vs frequency ω .

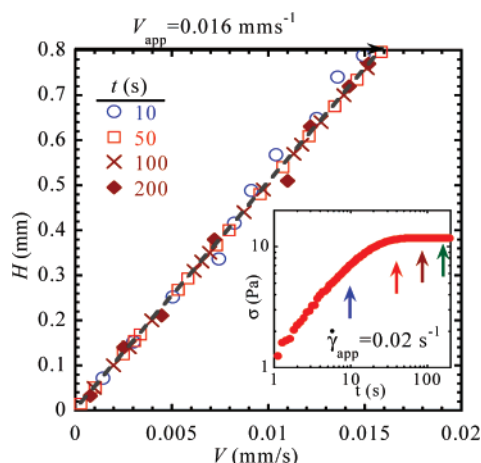


Figure 6. Velocity profiles at different times during a startup shear at $\dot{\gamma}_{app} = 0.02 s^{-1}$. The inset shows the stress response as a function of time.

B. Nonlinear Rheology. Both startup shear (controlled rate) and creep (controlled stress) modes were discretely applied to explore nonlinear rheological responses of the micellar solution. Figure 3 shows the shear stress growth as a function of time at low shear rates. With $\dot{\gamma}_{app} < \tau^{-1}$, the growth is monotonic. Beyond $\dot{\gamma}_{app} = 0.05 s^{-1}$, a stress overshoot emerges. At high shear rates with $\dot{\gamma}_{app} > 2.0 s^{-1}$, a cusp develops as shown in Figure 3, in sharp contrast to the smooth stress overshoot commonly seen in entangled polymer solutions. Upon plotting the stress growth $\sigma(\gamma)$ vs the elapsed strain γ , we see the stress maxima all occurring at $\gamma_b \approx 4.0$ as revealed by the inset of Figure 3. Such a feature has been reported before.^{13,18} It was proposed¹⁸ that this behavior is associated with finite extensibility of the micellar network.

During a creep experiment, the rise of the apparent shear rate $\dot{\gamma}_{app}$ as a function of time is reminiscent of a similar phenomenon in entangled polymer solutions.⁵³ Contrary to the case of polymer solutions where special efforts had to be made to ensure absence of any edge effect⁵⁴ on the characteristic rise, our micellar solution is so soft that it is entirely free of any edge fracture. In other words, the observed increase of the apparent shear rate as shown in Figure 4 is a true rheological response to the imposed shear stress. At low shear stress $\sigma < 20$ Pa, $\dot{\gamma}_{app}$

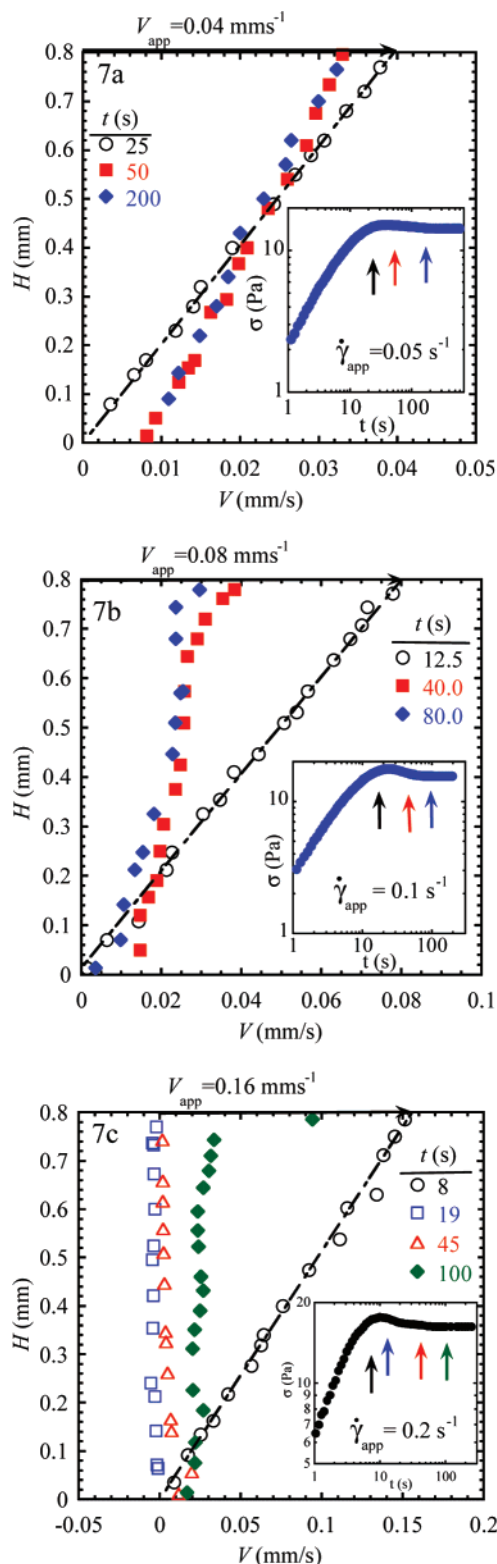


Figure 7. Transient and steady states at intermediate shear rates ranging from 0.05 to 0.2 s^{-1} , where the insets show the stress as a function of time: (a) velocity profiles at $\dot{\gamma}_{\text{app}} = 0.05 \text{ s}^{-1}$; (b) velocity profiles at $\dot{\gamma}_{\text{app}} = 0.1 \text{ s}^{-1}$; (c) velocity profiles at $\dot{\gamma}_{\text{app}} = 0.2 \text{ s}^{-1}$.

reaches steady state within 10 s or so. At $\sigma = 20 \text{ Pa}$, $\dot{\gamma}_{\text{app}}$ gradually increases to reach a steady-state value after $t \sim 200 \text{ s}$. Taking the steady-state value of σ , $\dot{\gamma}_{\text{app}}$, and $\eta_{\text{app}} = \sigma / \dot{\gamma}_{\text{app}}$ from both startup shear and creep measurements, we can plot the flow curves in Figure 5. A stress plateau characteristic is clearly seen in Figure 5, in accord with the literature.

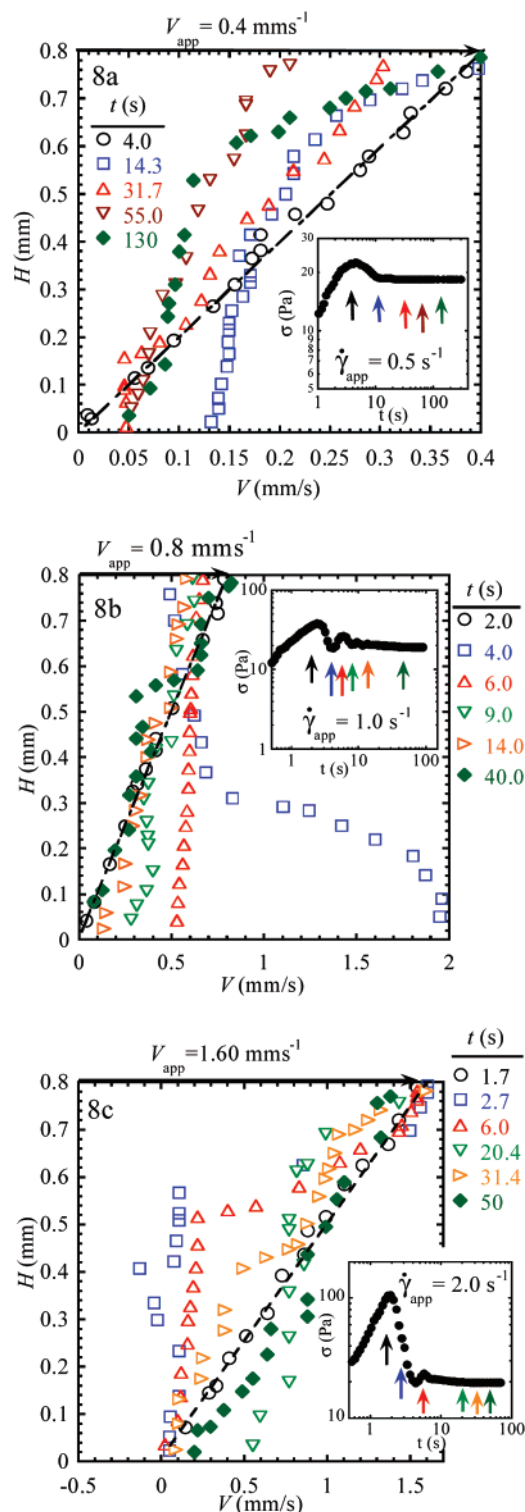


Figure 8. Transient and steady states at higher shear rates ranging from 0.5 to 2.0 s^{-1} , where the insets show the stress as a function of time: (a) velocity profiles at $\dot{\gamma}_{\text{app}} = 0.5 \text{ s}^{-1}$; (b) velocity profiles at $\dot{\gamma}_{\text{app}} = 1.0 \text{ s}^{-1}$; (c) velocity profiles at $\dot{\gamma}_{\text{app}} = 2.0 \text{ s}^{-1}$.

C. Startup Shear—PTV Measurements. 1. Homogeneous Flow in Terminal Regime ($\dot{\gamma}_{\text{app}} < \tau^{-1}$). At sufficiently low shear rates, there is no stress overshoot upon startup shear. Figure 6 shows that the velocity profile is fairly linear across the gap at all times. This result is consistent with an earlier report of sheared micellar solutions.⁴¹

2. Sliplike Behavior beyond the Terminal Regime. Beyond the terminal regime with $0.05 \leq \dot{\gamma}_{\text{app}} \leq 0.2 \text{ s}^{-1}$, a stress

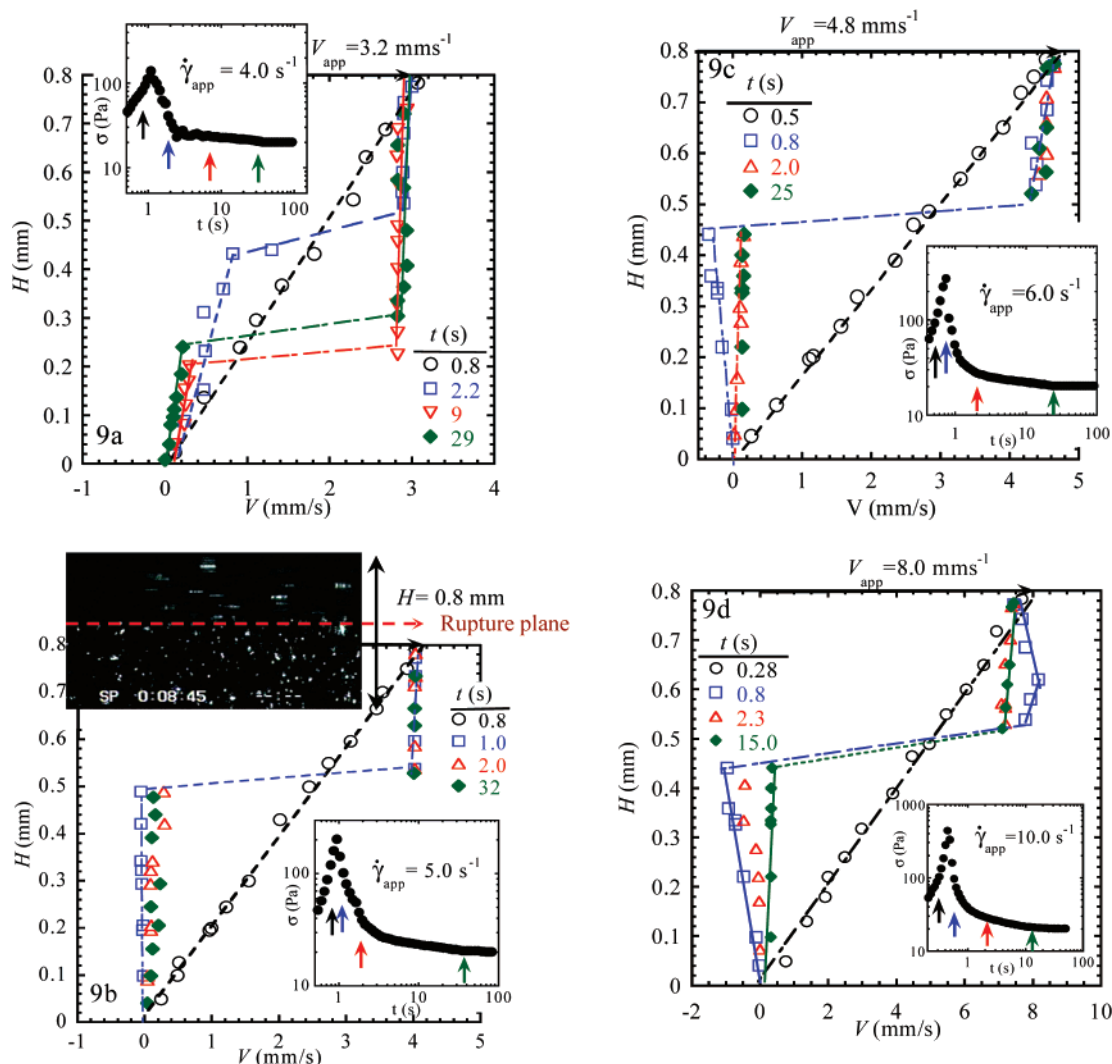


Figure 9. Transient and steady states at sufficiently high shear rates ranging from 4.0 to 10.0 s^{-1} , where the insets show the stress as a function of time: (a) velocity profiles at $\dot{\gamma}_{app} = 4.0 \text{ s}^{-1}$; (b) velocity profiles at $\dot{\gamma}_{app} = 5.0 \text{ s}^{-1}$, where the upper left corner inset shows a snap shot of particle movements after rupture in the sample interior; (c) velocity profiles at $\dot{\gamma}_{app} = 6.0 \text{ s}^{-1}$; (d) velocity profiles at $\dot{\gamma}_{app} = 10.0 \text{ s}^{-1}$.

overshoot is observed. Figure 7a–c shows the time-dependent velocity profiles upon startup shear. Before stress overshoot, the velocity profile is linear across the gap. After stress overshoot, interfacial wall slip is clearly the dominant mechanism causing the stress decline. These PTV observations offer useful insight into the origin of the stress plateau: the shear rate stays as low as 0.02 s^{-1} in the bulk even though the apparent rate can be many times higher, due to massive wall slip. The aqueous micellar solution is capable of such true interfacial slip because of the low solvent viscosity of water around $10^{-3} \text{ Pa}\cdot\text{s}$. We can estimate the slip length b and compare it with the sample thickness (ca. 1 mm). Inserting $\eta = 100 \text{ Pa}\cdot\text{s}$ from Figure 2 into the formula⁵⁵ $b = (\eta/\eta_i)a_L$, along with $\eta_i = 10^{-3} \text{ Pa}\cdot\text{s}$, and estimating slip layer to have a thickness of the mesh size of the entanglement network given by $(k_B T/G_p)^{1/3}$, we have $b \sim 3 \text{ mm}$.

3. Fluctuation of Velocity Profiles at Intermediate Rates. At higher shear rates with $\dot{\gamma}_{app} > 0.5 \text{ s}^{-1}$, the velocity profile is found to fluctuate across the gap after stress overshoot, as revealed by our PTV observations in Figure 8a–c. At $\dot{\gamma}_{app} = 1.0$ and 2.0 s^{-1} , a striking elastic recoil-like breakup either close to the wall or in the bulk accompanies the stress decline beyond the stress maximum. The velocity profile continues to be time dependent at long times.

4. Rupturelike Behavior at High Shear Rates. At sufficiently high shear rates, i.e., $\dot{\gamma}_{app} \geq 4.0 \text{ s}^{-1}$, the shear stress grows sharply as a function of time and declines drastically after reaching the stress peak. Our PTV observations show that the sharp drop in shear stress appears to stem from rupture of the sample in the bulk, as shown in Figure 9a–d where a “crack” emerges in the sample interior. At $\dot{\gamma}_{app} = 4.0 \text{ s}^{-1}$, the location of the “fault plane” is unstable and keeps changing. During this initial period, the stress signal also fluctuates as shown in the inset of Figure 9a. At a higher shear rate $\dot{\gamma}_{app} > 4.0 \text{ s}^{-1}$, the velocity profile appears more steady in contrast. Figure 9b–d presents the time evolution of velocity profiles at several different stages for $\dot{\gamma}_{app} = 5, 6$, and 10 s^{-1} , respectively. The inset of Figure 9b shows the snapshot of particle movements when the “crack” emerged in the middle of sample thickness at $\dot{\gamma}_{app} = 5.0 \text{ s}^{-1}$ at ca. 15 s. This image clearly shows that half of the sample close to the bottom stationary plate suffered negligible deformation and another half close to the upper rotating plate moved with a velocity compared to the speed of the top plate. Note the particles in the top half of the sample are line-shaped streaks because during the camera exposure time of $1/60 \text{ s}$ the particles traveled a distance equal to the streak length.

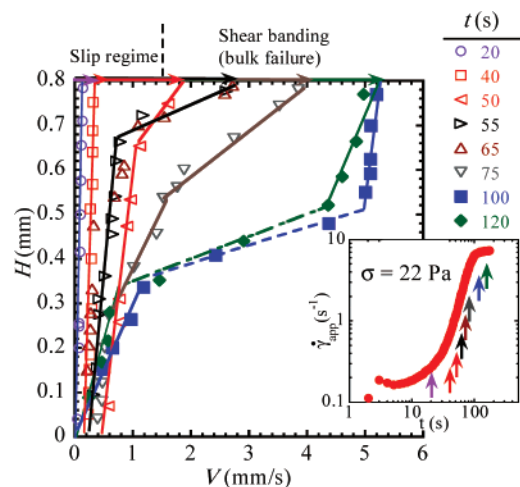


Figure 10. Time evolution of the velocity profile during creep at $\sigma = 22$ Pa. The inset shows the growth of $\dot{\gamma}_{app}$ as a function of time under constant $\sigma = 22$ Pa.

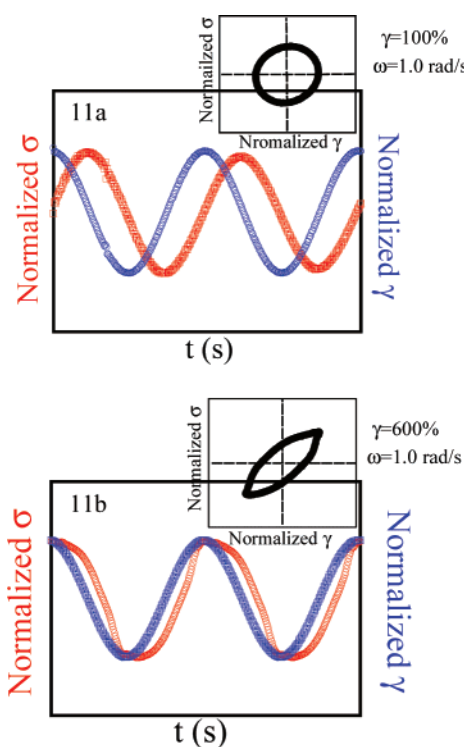


Figure 11. Normalized stress and strain signal as a function of time in steady state at different amplitude: (a) $\gamma = 100\%$, $\omega = 1.0$ rad/s; (b) $\gamma = 600\%$, $\omega = 1.0$ rad/s. The insets show the Lissajous patterns for each case.

D. Creep Mode—PTV Measurements. Figure 10 shows typical transient behavior of the micellar solution undergoing creep at a constant stress. At $\sigma = 22$ Pa, initially at $t = 20$ – 30 s, the sample suffers measurable wall slip. After $t = 40$ s, $\dot{\gamma}_{app}$ rises sharply. At $t = 50$ – 75 s, shear banding develops internally and evolves in time as the apparent shear rate further rises. Finally, at $t = 100$ s, a layer of higher local shear rate forms and $\dot{\gamma}_{app}$ saturate to a steady-state value around 6.5 s^{-1} . Figure 10 contrasts Figure 9b–d in that the severe rupturelike profile is absent in the creep mode. In other words, although both modes of shear produce nearly the same flow curves as shown in Figure 5, the velocity profiles and corresponding fluid structures are rather different. This difference is related to the fact that imposed constant shear stress of 22 Pa in creep is much lower than the peak stress of almost 300 Pa (read from Figure 9c) experienced

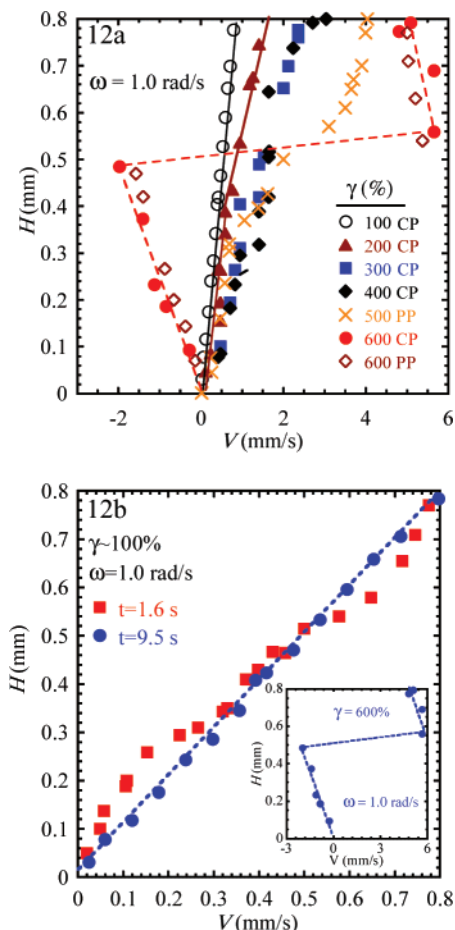


Figure 12. (a) Velocity profile at $\omega = 1.0$ rad/s in different amplitude strains ranging from 100% to 600% in both cone-plate and parallel plate geometries. (b) Transient behavior of velocity profile after the amplitude strain is suddenly lowered from 600% to 100% at $\omega = 1.0$ rad/s. The inset shows the steady-state rupturelike velocity profile during the preceding LAOS at $\gamma = 600\%$.

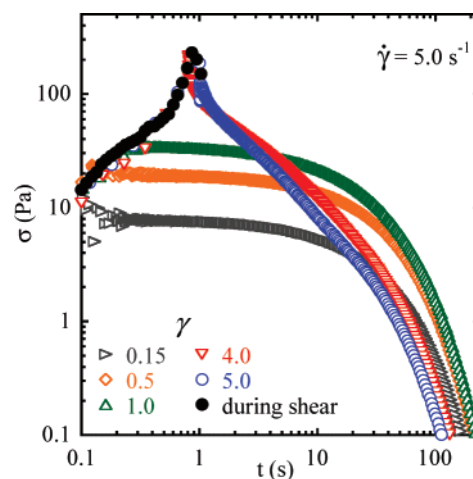


Figure 13. Shear stress growth and relaxation during and after discrete step strains ranging from 0.15 to 5.0 at $\dot{\gamma}_{app} = 5.0$ s^{-1} .

by the sample during startup shear at a rate corresponding to the final rate observed in creep.

E. Large-Amplitude Oscillatory Shear (LAOS). 1. Lissajous Pattern. Large-amplitude oscillatory (LAOS) has been employed widely to explore nonlinear rheology of complex fluids. We carried out LAOS experiments at a fixed frequency $\omega = 1.0$ rad/s (\gg crossover frequency $\omega_c \approx 0.03$ rad/s) and various strain amplitude from $\gamma = 0.4$ to 6.0. Figure 11a,b

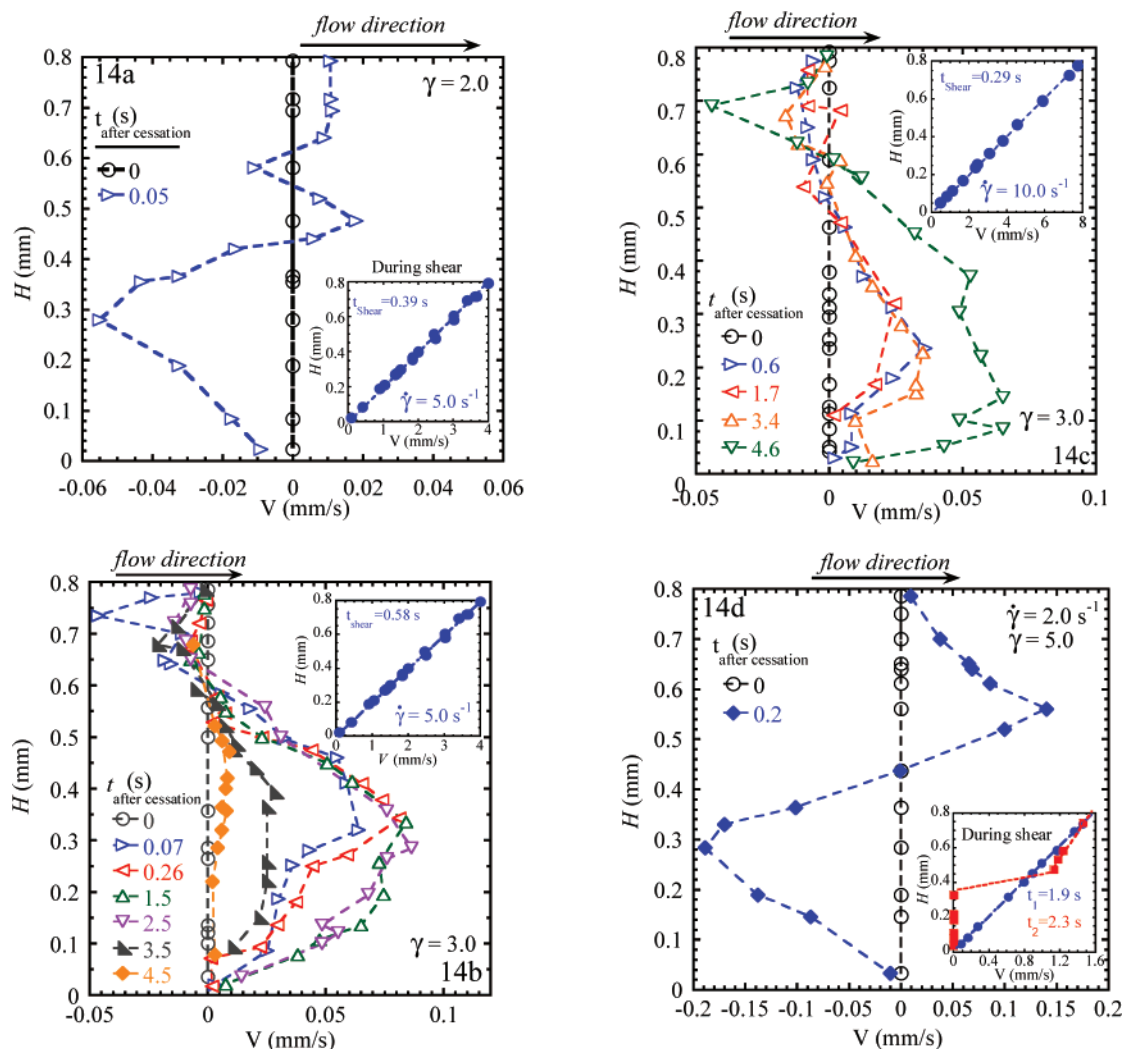


Figure 14. PTV measurements of macroscopic motions during relaxation for (a) $\gamma = 2.0$ at $\dot{\gamma}_{app} = 5.0 \text{ s}^{-1}$, (b) $\gamma = 3.0$ at $\dot{\gamma}_{app} = 5.0 \text{ s}^{-1}$, (c) $\gamma = 3.0$ at $\dot{\gamma}_{app} = 10.0 \text{ s}^{-1}$, and (d) $\gamma = 5.0$ at $\dot{\gamma}_{app} = 2.0 \text{ s}^{-1}$. The insets show the velocity profile during shear.

summarizes the normalized oscillatory shear stress and strain as a function of time and corresponding Lissajous pattern of CTAB/NaSal in steady state. Up to strain amplitude of 100%, the oscillatory stress is sinusoidal and the Lissajous plot is elliptical. As the strain amplitude increases, the shape of Lissajous pattern is distorted as the stress curve becomes nonsinusoidal and sawtooth-shaped. For example, Figure 11b for $\gamma = 600\%$ contrasts Figure 11a to suggest that nonlinear flow response emerges for $\gamma = 600\%$. Often such rheological information has been taken as intrinsic material responses to LAOS that are homogeneous across the sample thickness. It is crucial to verify whether uniform deformation prevails or not.

2. PTV Measurements. Figure 12a shows the PTV measurements of LAOS at different amplitudes all at the maximum of angular velocities in the steady state. At low strain amplitudes $\gamma \leq 100\%$, the velocity profile is fairly linear across the gap at $\omega = 1.0 \text{ rad/s}$. With $\gamma > 1.0$, nonuniform flow was visualized across the gap. Beyond the strain amplitude of 500%, the sample catastrophically ruptures, reminiscent of the features observed in startup shear. Comparison between cone–plate and parallel plate geometry in Figure 12a indicates that the effect of a stress gradient across the gap in cone–plate geometry is negligible. In a different LAOS experiment, the sample was first subjected to LAOS with $\gamma = 600\%$ at $\omega = 1.0 \text{ rad/s}$ and suffered rupturelike breakup across the sample thickness. Then, the strain

amplitude is suddenly lowered to 100% at the same frequency. Within a quarter of a cycle, i.e., in about 1.6 s, the sample almost returned to uniform shear. The velocity profile is completely linear after 3/2 cycle at 9.5 s, as shown in Figure 12b.

F. Step Strain. 1. Conventional Rheometric Measurements. Step strain experiments are conceptually the simplest. In a similar entangled wormlike micellar CTAB solution, failure of the Lodge–Meissner relation has been reported for large step strains.¹⁷ The reason for the breakdown of the Lodge–Meissner relation has been elusive. Here we make PTV and FB measurements to explore nonlinear responses of the CTAB micellar solution during and after step shear. Figure 13 shows the shear stress σ as a function of time for a range of γ from 0.15 to 5.0 at $\dot{\gamma}_{app} = 5.0 \text{ s}^{-1}$. There is a sharp contrast of stress relaxation behavior depending on whether γ is below 1.0 or well above 1.0.

2. PTV Measurements. Our PTV observations indicate that the sample does not relax quiescently beyond strain $\gamma \sim 1.5$ during relaxation. For example, after a step shear of $\gamma = 2.0$, we see significant macroscopic motions as shown in Figure 14a,b although the shear deformation took place uniformly across the gap. The observed recoil-like motions is reminiscent of similar phenomena found in entangled polymer solutions.^{50,51} It appears that this wormlike entangled micellar solution also suffered an elastically driven structural failure as entangled polymer solutions do⁵² upon large step strains. Nevertheless,

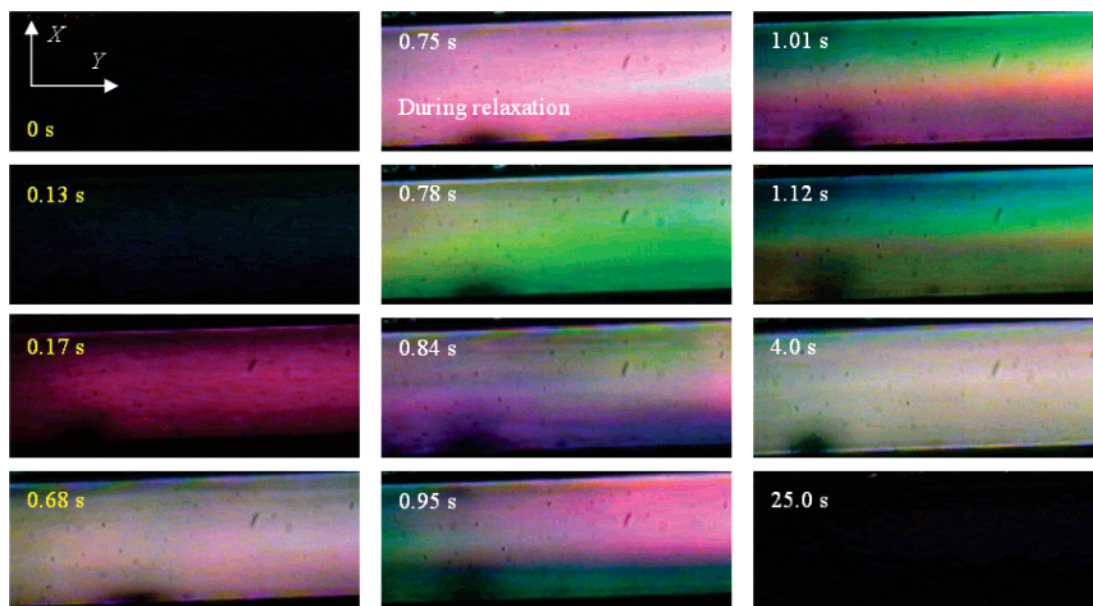


Figure 15. FB visualization from velocity gradient (X – Y) plane between crossed polarizers during shear and after shear with $V/H = 5.0 \text{ s}^{-1}$ and $H = 0.6 \text{ mm}$ up to $V\Delta t/H = 3.4$, i.e., up to $\Delta t = 0.68 \text{ s}$.

there is one remarkable difference between entangled micellar and polymer solutions. Unlike polymer solutions, the micellar solution exhibits accelerated macroscopic motions upon shear cessation. In other words, it takes a noticeable amount of time for the macroscopic motion to attain a maximum velocity as shown in Figure 14c. In other words, the recoil-like motions take a noticeable amount of time to accelerate before reaching a maximum velocity. It is plausible that micellar breakup process modified the overall dynamics of the failure process. Finally, we note that at amplitudes higher than $\gamma = 4.0$, the sample would break up internally during shear, as shown in the inset of Figure 14d. Upon shear cessation, recoil immediately occurs at the location of the breakup.

3. FB Visualization during Relaxation. Figure 15 shows the FB images during and after a step shear of $\gamma \approx 3.4$ at $\dot{\gamma}_{\text{app}} = 5 \text{ s}^{-1}$ in the velocity–gradient (X – Y) plane (in a setup depicted in Figure 1b). Uniform color was observed during shear, indicating that sample experienced uniform deformation up to 0.68 s . Upon shear cessation, inhomogeneous retardation emerges during relaxation ($t \approx 0.78$ – 3.0 s). This period of time corresponds to nonquiescent relaxation of the sample as observed by PTV. At $t = 4.0 \text{ s}$, the FB returned to uniform color and the sample fully relaxed at $t = 25.0 \text{ s}$. These FB observations are consistent with the preceding PTV observations.

In order to probe whether the sample recoil after step shear occurs uniformly throughout the sample, we have carried out simple flow birefringence observations using a setup depicted in Figure 1c. Figure 16a shows the retardation before, during, and after a step strain of $\gamma = 2.5$ at $\dot{\gamma}_{\text{app}} = 6.6 \text{ s}^{-1}$, as viewed along the velocity gradient direction, i.e., in the shear–vorticity (X – Z) plane. Before shearing, the color was uniformly blue, which was due to a full-wave retardation plate placed perpendicular to the shearing direction in between the two crossed polarizers. As the sample was undergoing uniform deformation up to $\gamma = 2.5$, the color moved backward along the Michel–Levy charter toward smaller values of apparent retardation due to the cancellation of the growing sample retardation against the retardation plate, and an orange color appeared at $\gamma = 2.5$. Upon shear cessation, blue patches emerged against a pinkish background, which reflects weaker retardation of the relaxing sample as the colors all move toward the deep blue color

corresponding to the equilibrium state in presence of the retardation plate. The blue patches, which correspond to a partially relaxed state, grew in a pink background, indicating the sample was not relaxing uniformly in the X – Z plane.

Figure 16b depicts the time-dependent retardation during shear at $\dot{\gamma}_{\text{app}} = 6.6 \text{ s}^{-1}$ up to $t = 1.5 \text{ s}$. After initial uniform deformation, uneven colors emerge beyond $\gamma = 4.0$ (corresponding to $t = 0.61 \text{ s}$), where the sample rupture would take place according to Figure 3 and Figure 9c. Accompanying the nonuniform distribution of color, the sample’s retardation decreases during a period from $t = 0.61$ to 1.5 s , indicating a drop in the level of normal force due to the rupture like recoil observed in Figure 9c,d. Upon flow cessation, it took more than 10 s for the system to return to its birefringence-free state as depicted by the first photo. It is important to note that, without crossed polarizers and retardation plate, these domains would be invisible. Thus, our flow birefringence observations have for the first time allowed us to visualize nonuniform fluid structure not only in the gap direction but also in the flow–vorticity plane during startup shear.

IV. Summary

We have carried out a combination of rheometric, particle tracking velocimetric, and flow birefringence observations of a CTAB/NaSal solution subjected to various forms of shear flow. In the terminal flow regime with $\dot{\gamma}_{\text{app}} < 0.02 \text{ s}^{-1}$, homogeneous flow was observed. At intermediate shear rates from 0.05 to 0.2 s^{-1} , stress overshoot similar to that in entangled polymer solutions was actually associated with wall slip. At higher shear rates ranging from 0.5 to 2.0 s^{-1} , nonlinear velocity profiles had considerable fluctuation after stress overshoot. At sufficient high shear rates $\dot{\gamma}_{\text{app}} > 4.0 \text{ s}^{-1}$, this sample yielded dramatically beyond $\gamma_b \approx 4.0$ with rupturelike response whose origin appears to be related to chain scission in the entanglement network of wormlike micelles. Shear inhomogeneity was also observed in LAOS and creep flow. Moreover, step shear with strains between 1.5 and 4.0 produced uniform deformation during shear as confirmed by PTV and FB observations. But upon shear cessation, nonuniform macroscopic motions occur as indicated by PTV measurements. The flow birefringence observations both across and along the sample thickness reveal that the

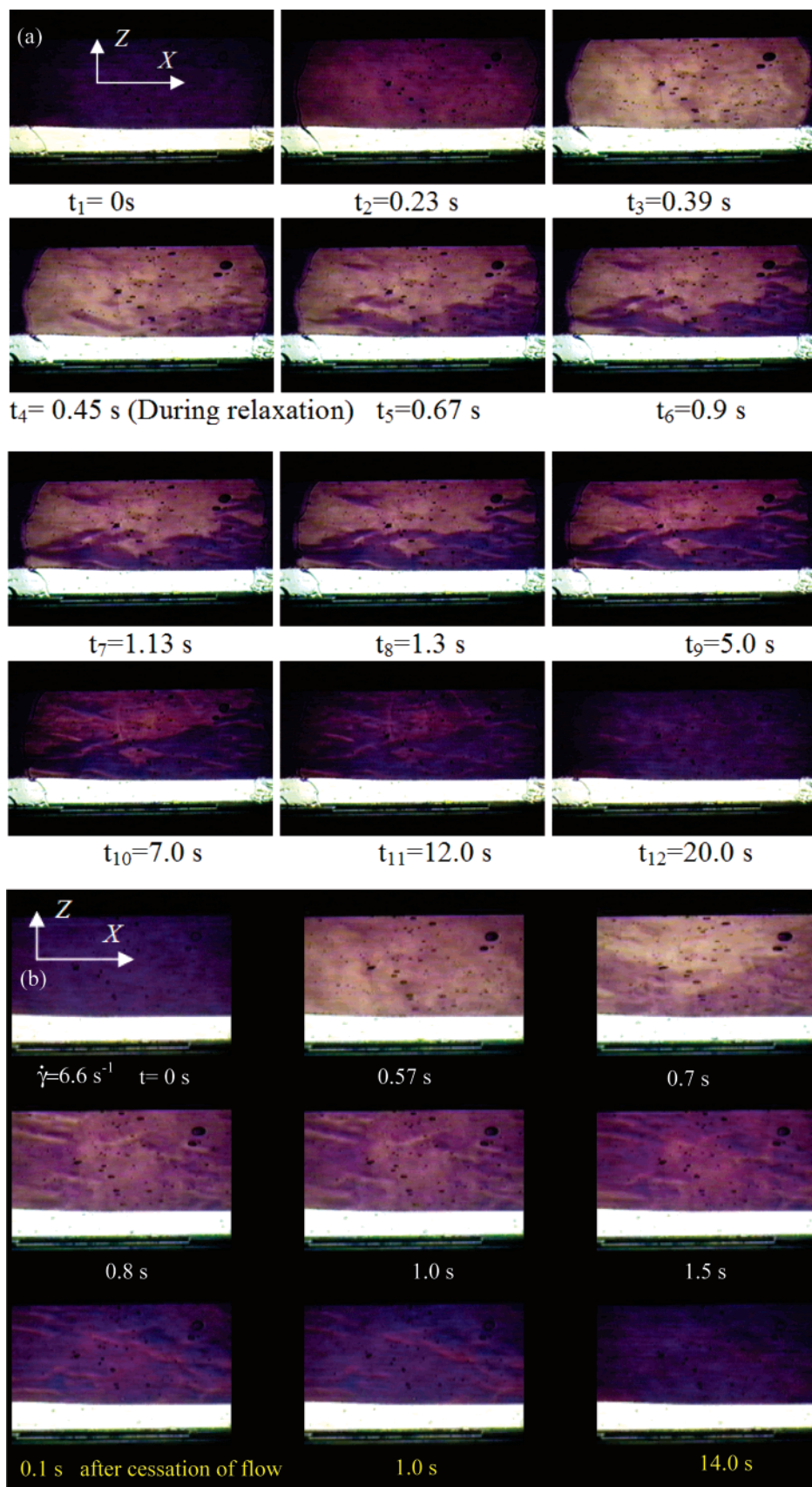


Figure 16. FB visualization from vorticity (X - Z) plane during shear and relaxation between crossed polarizers and a retardation film with $V/H = 6.6\text{ s}^{-1}$ and $H = 0.6\text{ mm}$: (a) up to $\Delta t = 0.38\text{ s}$, i.e., up to a strain of $V\Delta t/H = 2.5$, well before stress maximum is reached, and (b) up to $\Delta t = 1.5\text{ s}$, i.e., a strain of $V\Delta t/H = 10$, where the stress cusp is expected to occur at a strain of 4.0 according to the inset of Figure 3, i.e., at $t = 0.61\text{ s}$. Uneven color due to emergence of “patches” can be seen after the frame of 0.57 s .

structural breakdown occurred nonuniformly three dimensionally. Since the spatial distribution of the PTV particles remains

random and thus unchanged during any of these different forms of shear, we have no reason to suggest that the observed shear

banding is caused by presence of the particles. Notably, previous NMR imaging studies^{33–37} that did not involve inclusion of particles also reported shear banding in similar wormlike micellar solutions.

Acknowledgment. The authors thank W. R. Burghardt for bringing the experimental system of ref 17 to our attention. This work is supported, in part, by a small grant for exploratory research from National Science Foundation (DMR-0603951) and by a PRF grant from American Chemical Society (#40596-AC7).

References and Notes

- (1) Israelachvili, J. *Intermolecular and Surface Forces*, 2nd ed.; Academic Press: San Diego, CA, 1992.
- (2) Stones, P. A.; Hudson, S. D.; Dalhaimer, P.; Discher, D. E.; Amis, E. J.; Migler, K. B. *Macromolecules* **2006**, *39*, 7144.
- (3) For a review see: Cates, M. *Adv. Phys.* **2006**, *55*, 799.
- (4) Cates, M. E. *Macromolecules* **1987**, *20*, 2289.
- (5) Turner, M. S.; Cates, M. E. *Langmuir* **1991**, *7*, 1590.
- (6) Rehage, H.; Hoffmann, H. *J. Phys. Chem.* **1988**, *92*, 4712.
- (7) Rehage, H.; Hoffmann, H. *Mol. Phys.* **1991**, *74*, 933.
- (8) Berret, J. F.; Appell, J.; Porte, G. *Langmuir* **1993**, *9*, 2851.
- (9) Berret, J. F.; Roux, D. C.; Porte, G.; Linder, P. *Europhys. Lett.* **1994**, *25*, 521.
- (10) Shikata, T.; Hirata, H.; Kotaka, T. *Langmuir* **1987**, *3*, 1081.
- (11) Shikata, T.; Hirata, H.; Kotaka, T. *Langmuir* **1988**, *4*, 354.
- (12) Shikata, T.; Hirata, H.; Kotaka, T. *Langmuir* **1989**, *5*, 398.
- (13) Shikata, T.; Hirata, H.; Takatori, E.; Osaki, K. *J. Non-Newtonian Fluid Mech.* **1988**, *28*, 171.
- (14) Candau, S. J.; Hirsch, E.; Zana, R.; Delsanti, M. *Langmuir* **1989**, *5*, 1225.
- (15) Kern, F.; Zana, R.; Candau, J. *Langmuir* **1991**, *7*, 1344.
- (16) Shikata, T.; Dahman, S. J.; Pearson, D. S. *Langmuir* **1994**, *10*, 3470.
- (17) Brown, E. F.; Burghardt, W. R.; Venerus, D. C. *Langmuir* **1997**, *13*, 3902.
- (18) Inoue, T.; Inoue, Y.; Watanabe, H. *Langmuir* **2005**, *21*, 1201.
- (19) Spenley, N. A.; Cates, M. E.; McLeish, T. C. B. *Phys. Rev. Lett.* **1993**, *71*, 939.
- (20) Doi, M.; Edwards, S. F. *J. Chem. Soc., Faraday Trans. 2* **1979**, *75*, 38.
- (21) Cates, M. E.; McLeish, T. C. B.; Marrucci, G. *Europhys. Lett.* **1993**, *21*, 451.
- (22) Cappelaere, E.; Cressely, R.; Decruppe, J. P. *Colloids Surf.* **1995**, *104*, 353.
- (23) Decruppe, J. P.; Cressely, R.; Makhloufi, E.; Cappelaere, E. *Colloid Polym. Sci.* **1995**, *273*, 346.
- (24) Makhloufi, E.; Decruppe, J. P.; Ait-Ali, A.; Cressely, R. *Europhys. Lett.* **1995**, *32*, 253.
- (25) Roux, D. C. J.; Berret, J. F.; Porte, E.; Peuvrel-disdier, E.; Linder, P. *Macromolecules* **1995**, *28*, 1681.
- (26) Berret, J. F. *Langmuir* **1997**, *13*, 2227.
- (27) Cappelaere, E.; Berret, J. F.; Decruppe, J. P.; Cressely, R.; Linder, P. *Phys. Rev. E* **1997**, *56*, 1869.
- (28) Berret, J. F.; Roux, D. C.; Linder, P. *Eur. Phys. J. B* **1998**, *5*, 67.
- (29) Lee, J. Y.; Fuller, G. G.; Hudson, N. E.; Yuan, Y. F. *J. Rheol.* **2005**, *49*, 535.
- (30) Lerouge, S.; Decruppe, J. P.; Olmsted, P. *Langmuir* **2004**, *20*, 11355.
- (31) Drappier, J.; Bonn, D.; Meunier, J.; Lerouge, S.; Decruppe, J. P.; Bertnad, F. *J. Stat. Mech. Theory E* **2006**, *4*, 04003.
- (32) Callaghan, P. T.; et al. *J. Phys. II* **1996**, *6*, 375.
- (33) Mair, R. W.; Callaghan, P. T. *Europhys. Lett.* **1996**, *36*, 719.
- (34) Britton, M. M.; Callaghan, P. T. *Phys. Rev. Lett.* **1997**, *30*, 4930.
- (35) Britton, M. M.; Mair, R. W.; Lambert, R. K.; Callaghan, P. T. *J. Rheol.* **1999**, *43*, 897.
- (36) Fischer, E.; Callaghan, P. T. *Europhys. Lett.* **2000**, *50*, 803.
- (37) Fischer, E.; Callaghan, P. T. *Phys. Rev. E* **2001**, *64*, 011501.
- (38) Salmon, J. B.; Colin, A.; Manneville, S.; Molino, F. *Phys. Rev. Lett.* **2003**, *90*, 228303.
- (39) Salmon, J. B.; Manneville, S.; Colin, A. *Phys. Rev. E* **2003**, *68*, 051503.
- (40) Becu, L.; Manneville, S.; Colin, A. *Phys. Rev. Lett.* **2004**, *93*, 018301.
- (41) Hu, Y. T.; Lips, A. *J. Rheol.* **2005**, *49*, 1001.
- (42) Lopez-Gonzalez, M. R.; Holmes, W. M.; Callaghan, P. T. *Soft Matter* **2006**, *2*, 855.
- (43) Menezes, E. V.; Graessley, W. W. *J. Polym. Sci., Polym. Phys. Ed.* **1982**, *20*, 1817.
- (44) Bercea, M.; Peiti, C.; Simionescu, B.; Navard, P. *Macromolecules* **1993**, *26*, 7095.
- (45) Graham, R. S.; et al. *J. Rheol.* **2003**, *47*, 1171.
- (46) Tapadia, P.; Wang, S. Q. *Phys. Rev. Lett.* **2006**, *96*, 016001.
- (47) Boukany, P. E.; Wang, S. Q. *J. Rheol.* **2007**, *51*, 217.
- (48) Tapadia, P.; Ravindranath, S.; Wang, S. Q. *Phys. Rev. Lett.* **2006**, *96*, 196001.
- (49) Ravindranath, S.; Wang, S. Q. *J. Rheol.*, submitted for publication.
- (50) Wang, S. Q.; et al. *Phys. Rev. Lett.* **2006**, *97*, 187801.
- (51) Ravindranath, S.; Wang, S. Q. *Macromolecules* **2007**, *40*, 8031.
- (52) Wang, S. Q.; Ravindranath, S.; Wang, Y.; Boukany, P. E. *J. Chem. Phys.* **2007**, *127*, 064903.
- (53) Tapadia, P.; Wang, S. Q. *Macromolecules* **2004**, *37*, 9083.
- (54) Ravindranath, S.; Wang, S. Q. *J. Rheol.*, submitted for publication (2007).
- (55) Wang, S. Q. *Adv. Polym. Sci.* **1999**, *138*, 227.

MA702527S